

# Magnetic spectrum of trigonally warped bilayer graphene: Semiclassical analysis, zero modes, and topological winding numbers

R. de Gail, M. O. Goerbig, and G. Montambaux

*Laboratoire de Physique des Solides, CNRS UMR 8502, Université Paris-Sud, F-91405 Orsay cedex, France*

(Received 19 March 2012; revised manuscript received 20 June 2012; published 5 July 2012)

We investigate the fine structure in the energy spectrum of bilayer graphene in the presence of various stacking defaults, such as a translational or rotational mismatch. This fine structure consists of four Dirac points that move away from their original positions as a consequence of the mismatch and eventually merge in various manners. The different types of merging are described in terms of topological invariants (winding numbers) that determine the Landau-level spectrum in the presence of a magnetic field as well as the degeneracy of the levels. The Landau-level spectrum is, within a wide parameter range, well described by a semiclassical treatment that makes use of topological winding numbers. However, the latter need to be redefined at zero energy in the high-magnetic-field limit as well as in the vicinity of saddle points in the zero-field dispersion relation.

DOI: [10.1103/PhysRevB.86.045407](https://doi.org/10.1103/PhysRevB.86.045407)

PACS number(s): 73.43.Nq, 71.10.Pm, 73.20.Qt

## I. INTRODUCTION

Graphene research has stimulated many fields of condensed-matter physics during the last years.<sup>1</sup> One of the most remarkable of these fields is certainly the topological description of electronic energy bands, such as in the context of topological insulators.<sup>2,3</sup> Indeed, the low-energy electronic properties of a single graphene layer are determined by two particular band-contact points at the corners  $K$  and  $K'$  of the first Brillouin zone, with a linear dispersion relation (the so-called Dirac points). These Dirac points are associated with a topological Berry phase that stems from the winding of the phase in the electronic wave function on closed paths around these points—the Berry phase is then  $\pi$  times this winding number.<sup>4</sup> Prominent consequences of this Berry phase are the absence of backscattering in the case of long-range disorder,<sup>1</sup> Klein tunneling,<sup>5,6</sup> and a particular form of the Landau level (LL) spectrum in the presence of a magnetic field, with a topologically protected zero-energy level.<sup>7</sup>

Bilayer graphene, that is obtained from an AB stacking of two graphene layers, has an even richer band structure, also from a topological point of view, than monolayer graphene. Most of its electronic properties have successfully been described in the framework of two parabolic bands with opposite curvature that touch each other at the Fermi level. As compared to monolayer graphene, the winding number associated with these band-contact points is twice as large.<sup>8</sup> This gives rise to a twofold orbital degeneracy of the zero-energy level in the presence of a magnetic field, in addition to the fourfold spin-valley degeneracy, and thus to a particular series of Hall plateaus that have been observed in quantum-Hall measurements.<sup>9</sup> However, this picture is only approximately valid in an intermediate energy range (above  $\simeq 10$  meV), whereas subordinate hopping terms yield a fine structure in the energy spectrum (called “trigonal warping”), in the form of four Dirac points with linear dispersion, at lower energies.<sup>8</sup> This transition from four Dirac points, with unit winding numbers, to the parabolic regime with a winding number of 2 may be viewed as a finite-energy Lifshitz transition<sup>10</sup> between disconnected Fermi pockets at low energies and a simply connected Fermi sea (per valley) at higher energies.<sup>11</sup>

In contrast to earlier experiments on bilayer graphene, today’s availability of high-quality samples allows one to probe now this low-energy regime in which quantum-Hall measurements indicate the presence of additional Dirac points,<sup>12</sup> and it is noteworthy to mention that indications of Lifshitz transitions have been found in cyclotron-resonance measurements in graphite.<sup>13</sup>

The fine structure of the energy spectrum of bilayer graphene is also interesting from the point of view of stacking defaults, such as a displacement, strain, or a twist with respect to perfect AB stacking.<sup>14–16</sup> In this case, the low-energy dispersion is modified and two or more of the Dirac points may easily merge.<sup>15,17</sup> This needs to be contrasted to Dirac-point merging in monolayer graphene that has been extensively studied on the theoretical level<sup>18–23</sup> but that is difficult to achieve experimentally due to an enormous strain required.<sup>24</sup> Furthermore, moderate stacking defaults may allow for the systematic study of merging transitions that fall into two distinct topological classes,<sup>17</sup> whereas the merging of Dirac points with opposite winding numbers yields a gap in the band structure, that of Dirac points with the same winding number maintains the band-contact points. This difference has direct consequences for the LL spectrum, namely the zero-energy level. Whereas in the former case of merging Dirac points with opposite winding number, the twofold degeneracy of the zero-energy level is lifted,<sup>20</sup> it is topologically protected in the latter case.<sup>17</sup>

Here, we investigate the different merging transitions that one may encounter in bilayer graphene with a stacking default, within a continuum model that has been used both in the description of bilayer graphene with a mismatch described by a translation between the layers or under strain<sup>15,25</sup> as well as in that of a twisted bilayer.<sup>17</sup> This continuum model, which goes beyond the linear Dirac-point approximation, may be viewed as a continuum model of the second generation.<sup>26</sup> In addition to the merging transition between Dirac points of opposite winding number, we discuss in detail the triple merging of three Dirac points that has been investigated in previous theoretical works.<sup>15,25,27</sup> This triple merging happens to be unstable in the sense that it only occurs in the framework of a displacement or strain in a high-symmetry axis of the

lattice—a slight deviation from such an axis splits the triple merging into a usual merging transition of two Dirac points in a first step, followed by merging with the remaining Dirac point in a second step. As compared to previous studies of the LL spectrum for trigonally warped bilayer graphene,<sup>8,25</sup> we provide in the present paper a detailed semiclassical analysis of the spectrum. This analysis is based on winding numbers that allow for a transparent understanding of LL degeneracies and zero modes. Furthermore, we investigate quantum corrections beyond the semiclassical limit. Both at zero energy in the high-field limit and in the vicinity of saddle points in the dispersion relation, these corrections are relevant because they blur the semiclassical trajectories and thus call for a modification of the description in terms of winding numbers. This allows for an understanding of the change in the LL degeneracy at zero energy and in the vicinity of saddle points in the dispersion relation.

The paper is organized as follows. In Sec. II, we present the continuum model that accounts for the different stacking defaults in bilayer graphene and discuss the band structure and zero-field merging transitions in the several limits. Furthermore, we characterize the merging transitions in terms of topological winding numbers. Section III is devoted to the LL spectrum associated with the different merging transitions. The spectrum is obtained within a numerical solution of the quantum-mechanical eigenvalue equation (see Sec. III A) and analyzed in the framework of a semiclassical treatment (see Sec. III B). Topological aspects of the LL spectrum are discussed in Sec. IV, and a detailed discussion of the different aspects of the spectrum may be found in Sec. V, before we present our conclusions (see Sec. VI).

## II. BAND STRUCTURE OF DEFORMED BILAYER GRAPHENE

Bilayer graphene harbors different stacking geometries, pictured in Fig. 1, among which the energetically most favorable is the Bernal (AB) configuration in which a B sublattice atom of the first layer sits on top of an  $\tilde{A}$  sublattice atom of the second layer [see Fig. 1(a)]. This particular ordering is naturally observed in graphite, as well as for synthesized bilayer graphene. Other stackings may be described in terms of a rotation default<sup>26</sup> and a displacement vector<sup>15,25</sup> and may be observed in graphene samples, such as for example in epitaxial graphene on the C face of the SiC crystal.<sup>28</sup> We also consider strain constraints along both layers.<sup>25,29</sup>

### A. Tight-binding approach

For perfect AB stacking,<sup>8</sup> the tight-binding approximation yields a four-band Hamiltonian that may be written in the (A,B, $\tilde{A},\tilde{B}$ ) basis:

$$\mathcal{H}(\mathbf{k}) = \begin{pmatrix} 0 & t\gamma(\mathbf{k}) & 0 & t'\gamma^*(\mathbf{k}) \\ t\gamma^*(\mathbf{k}) & 0 & t_{\perp} & 0 \\ 0 & t_{\perp} & 0 & t\gamma(\mathbf{k}) \\ t'\gamma(\mathbf{k}) & 0 & t\gamma^*(\mathbf{k}) & 0 \end{pmatrix}, \quad (1)$$

where

$$\gamma(\mathbf{k}) = -(1 + e^{i\mathbf{k}\cdot\mathbf{a}_1} + e^{i\mathbf{k}\cdot\mathbf{a}_2}), \quad (2)$$

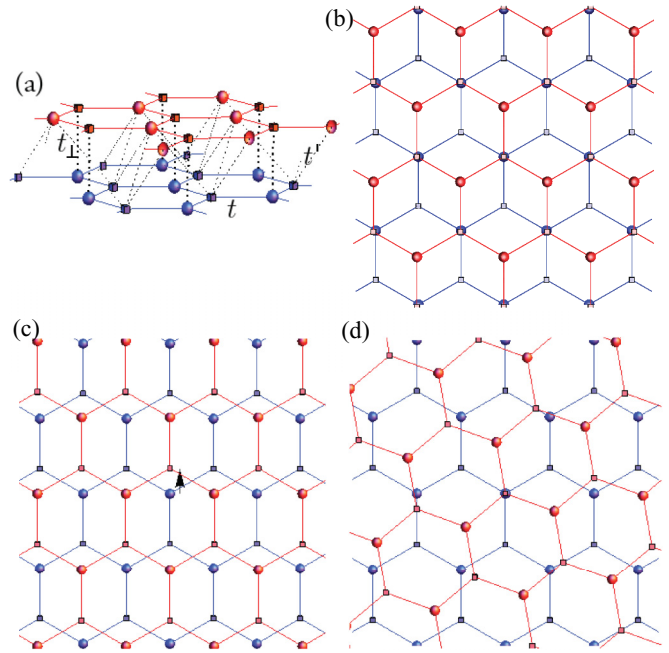


FIG. 1. (Color online) Lattice structure of the bilayer graphene. (a) Atomic structure around an elementary cell for the Bernal configuration with (A,B) atoms (first layer) in blue and ( $\tilde{A},\tilde{B}$ ) atoms (second layer) in red. Hopping parameters  $t$ ,  $t_{\perp}$ , and  $t'$  are also pictured. (b), (c), and (d) depict a planar lattice geometry for the Bernal, slided, and twisted bilayers, respectively.

and  $\mathbf{a}_1$ ,  $\mathbf{a}_2$  are elementary vectors of the triangular Bravais lattice,

$$\mathbf{a}_{1,2} = \frac{a}{2}(\pm\sqrt{3}\mathbf{e}_x + 3\mathbf{e}_y), \quad (3)$$

and  $a = 0.142$  nm is the distance between neighboring carbon atoms in the same layer. The hopping parameters can be experimentally evaluated,<sup>30</sup> and one obtains the hierarchy

$$t (\sim 3 \text{ eV}) \gg t_{\perp} (\sim 0.4 \text{ eV}) \gtrsim t' (\sim 0.3 \text{ eV}), \quad (4)$$

where  $t$  represents the hopping between  $p_z$  orbitals of nearest-neighbor carbon atoms within the same layer,  $t_{\perp}$  the perpendicular hopping amplitude between a B sublattice atom of one layer and the  $\tilde{A}$  atom of the other layer, and  $t'$  is the transfer integral from an A site of one layer to the nearest  $\tilde{B}$  sites of the other layer [see Fig. 1(a)]. All other orbital overlap may be neglected for energies larger than 1 meV.<sup>30</sup>

### B. Low-energy Hamiltonian

In the small-wave-vector limit ( $|\mathbf{q}| \ll 1/a$ ), Hamiltonian (1) may be expanded around a  $K$  or  $K'$  corner of the hexagonal Brillouin zone situated at the positions  $\pm\mathbf{K} = \pm 4\pi\mathbf{e}_x/3\sqrt{3}a$ , modulo a reciprocal lattice vector. One has then  $t\gamma(\pm\mathbf{K} + \mathbf{q}) \approx v_F(\pm q_x - iq_y)$ , in terms of the Fermi velocity  $v_F = 3ta/2$  ( $\hbar = 1$  henceforth) and  $q \ll K$ . Furthermore, for energies lower than  $t_{\perp}$ , only two bands are relevant, and they may be described with the help of an effective two-band continuum Hamiltonian:<sup>8</sup>

$$\mathcal{H}_K \approx b \begin{pmatrix} 0 & \pi^{\dagger 2} \\ \pi^2 & 0 \end{pmatrix} + c \begin{pmatrix} 0 & \pi \\ \pi^{\dagger} & 0 \end{pmatrix} = \mathcal{H}_b + \mathcal{H}_c. \quad (5)$$

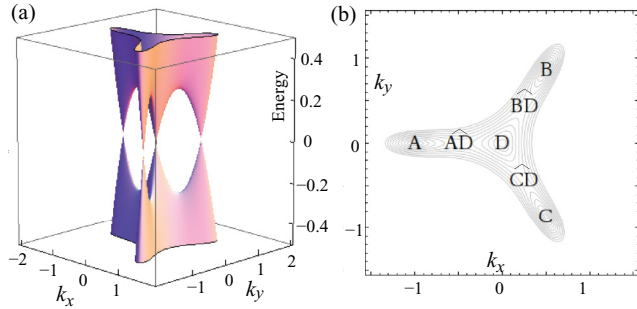


FIG. 2. (Color online) (a) Band structure of the perfectly AB stacked bilayer graphene around one of the valleys. (b) Position of the remarkable points in reciprocal space. We label the four Dirac cones from A to D and the corresponding saddle points  $\widehat{AD}$ ,  $\widehat{BD}$ , and  $\widehat{CD}$ . While the Dirac points all reside at zero energy, the saddle points have an energy  $E = c^2/4b$ . The wave vectors are measured in units of  $c/b$  and the energy in units of  $c^2/b$ .

Here,  $|b| = v_F^2/t_\perp \approx 14/m_0$ , in terms of the bare electron mass  $m_0$ ,  $c = v_F t'/t \approx 10^5$  m/s, and  $\pi = q_x + iq_y$  is the complex momentum operator in the continuum limit (that changes as  $\pi \rightarrow -\pi^\dagger$  when  $\mathbf{K} \rightarrow \mathbf{K}' = -\mathbf{K}$ ). The  $\mathcal{H}_b$  term in Eq. (5) is dominant for energies higher than  $\sim 10$  meV and lower than  $t_\perp \sim 0.4$  eV. In the absence of the term  $\mathcal{H}_c$ , it enforces a quadratic dispersion around the band-contact points at  $K$  and  $K'$ . For energies lower than  $\sim 10$  meV,  $\mathcal{H}_c$  becomes relevant and trigonally warps the band structure, which now presents four Dirac cones (see Fig. 2). One of the Dirac points ( $D$ ) remains at the center  $\mathbf{q} = 0$ , whereas three additional cones ( $A$ ,  $B$ , and  $C$ ) are arranged in a triangle around the first one.

### 1. Slide and strain deformation

The translational and strain constraints may be accounted for by adding a constant shift

$$\mathcal{H}_\Delta = \begin{pmatrix} 0 & -\Delta \\ -\Delta^* & 0 \end{pmatrix} \quad (6)$$

to Hamiltonian (5) that represents the only relevant perturbation whenever time-reversal and lattice-inversion symmetries are preserved.<sup>31</sup> Hence translation and strain constraints inevitably give rise to the term (6). For instance, a small sliding deformation renders the  $t'$  hopping anisotropic due to different orbital overlaps. In a similar fashion to the anisotropic honeycomb lattice problem,<sup>22,23</sup> the renormalized amplitude modifies the continuum approximation by shifting the momentum by a constant value  $\Delta$ ,

$$c\pi \rightarrow c\pi - \Delta. \quad (7)$$

The effective Hamiltonian

$$\mathcal{H}_T = \mathcal{H}_b + \mathcal{H}_c + \mathcal{H}_\Delta \quad (8)$$

was introduced in Ref. 15 to take into account a translational mismatch between the two graphene layers. A more microscopic discussion of the model may be found in Refs. 25 and 29.

## 2. Rotational default

In the case of a twisted (or rotationally faulted) bilayer, lattice-inversion symmetry is broken. For small and moderate twist angles, the model  $\mathcal{H}_b + \mathcal{H}_\Delta$  is an approximation that yields the correct shape of the energy spectrum and the right topological properties of the original system, such as the degeneracy of the zero-energy Landau level.<sup>17</sup> The full band structure requires taking into account the commensurability between the rotated layers and the resulting Moiré patterns.<sup>16</sup> Trigonal warping within the twisted bilayer system is likely to be negligible since the orbital mismatch renders all hopping parameters small compared to  $t$  or  $t_\perp$ , such that  $\mathcal{H}_c = 0$ . Notice furthermore that also  $t_\perp$  is significantly lowered by the twist. For this particular reason, we do not consider  $\mathcal{H}_T$  in Eq. (8) as a universal Hamiltonian for bilayer graphene but rather as a model that correctly interpolates between several configurations that exist under various experimental conditions. Notice that interaction effects generate the same distortion  $\mathcal{H}_\Delta$ , both with<sup>11</sup> and without<sup>32</sup> trigonal warping.

## C. Band structure

The band structure of  $\mathcal{H}_T$  in Eq. (8) is plotted in Fig. 3 for various values of  $\Delta$ .

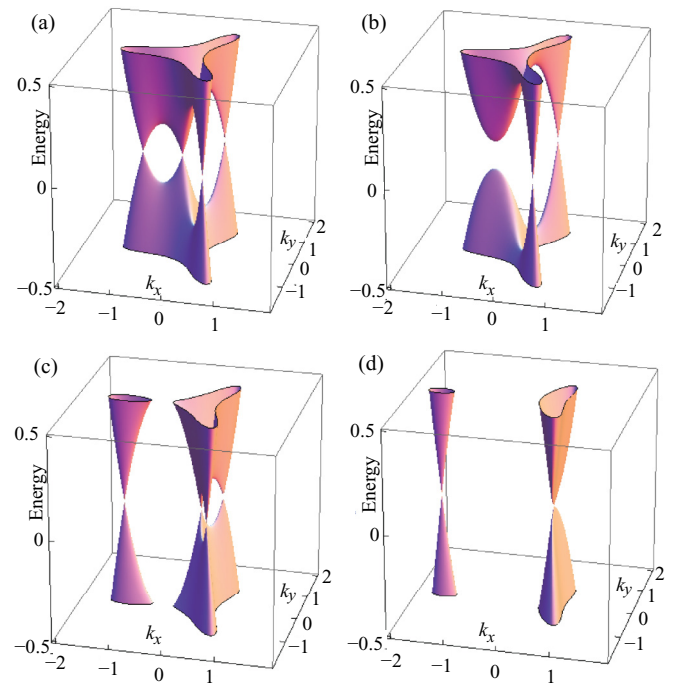


FIG. 3. (Color online) Band structure of bilayer graphene around the  $K$  valley for the Hamiltonian  $\mathcal{H}_\Delta$ , with a real value of  $\Delta$ . For  $\Delta < 0$ , the two cones  $D$  and  $A$  start to merge [panels (a), for  $\Delta = -0.1c^2/b$ ], and give rise to a local minimum after the merging transition, at  $\Delta = -c^2/4b$ , [panel (b) for a value of  $\Delta = -0.32c^2/b$ ]. The opposite case of  $\Delta > 0$  [panels (c) for  $\Delta = 0.3c^2/b$  and (d) for  $\Delta = 0.92c^2/b$ ], reveals the merging of three cones at a time,  $D$ ,  $B$ , and  $C$ , or triple merging. The wave vectors are measured in units of  $c/b$  and the energy in units of  $c^2/b$ .

### 1. Undistorted case

Without any distortion ( $\Delta = 0$ , see Fig. 2), the band structure is trigonally symmetric, with a central cone  $D$  and three peripheral ones,  $A$ ,  $B$ , and  $C$  positioned at

$$\begin{aligned} D &= (0,0), \quad A = \left(-\frac{c}{b}, 0\right), \\ B/C &= \left(\frac{c}{2b}, \pm \frac{\sqrt{3}c}{2b}\right), \end{aligned} \quad (9)$$

within a valley. A Taylor expansion of the energy dispersion around the four Dirac points yields

$$\begin{aligned} E_D(\mathbf{q}) &= c\sqrt{q_x^2 + q_y^2}, \\ E_A(\mathbf{q}) &= c\sqrt{q_x^2 + 9q_y^2}, \\ E_{B/C}(\mathbf{q}) &= c\sqrt{7q_x^2 + 3q_y^2} \pm 4\sqrt{3}q_xq_y, \end{aligned} \quad (10)$$

such that one may define averaged Fermi velocities, that is  $v_D = \sqrt{v_x v_y} = c$  for the  $D$  cone and  $v_A = v_B = v_C = \sqrt{3}c$  for the satellite ones.<sup>8</sup> Three saddle points join each peripheral cone to the central one, see Fig. 2, and are located at

$$\begin{aligned} \widehat{AD} &= \left(-\frac{c}{2b}, 0\right), \\ \widehat{BD}/\widehat{CD} &= \left(\frac{c}{4b}, \pm \frac{\sqrt{3}c}{4b}\right). \end{aligned} \quad (11)$$

As a consequence of the trigonal symmetry, they occur all at the same energy:

$$\begin{aligned} E_{\widehat{AD}} &= E_S = \frac{c^2}{4b}, \\ E_{\widehat{BD}} &= E_{\widehat{CD}} = E_{S'} = \frac{c^2}{4b}, \end{aligned} \quad (12)$$

that is

$$E_S = E_{S'} = \frac{1}{4} \left(\frac{t'}{t}\right)^2 t_{\perp} \simeq 1 \text{ meV}, \quad (13)$$

where we have used the values of Eq. (4) for the hopping amplitudes.

### 2. Deformation along an axis of high symmetry

The trigonal point-symmetry is broken as soon as  $\Delta \neq 0$ . We first consider the case of a real-valued constant, corresponding to an applied deformation along the  $y$  axis [see Fig. 1(c)], that is an axis of high symmetry. The Dirac cones are then moved from the positions (9) to

$$\begin{aligned} D &= \left(-\frac{c - \sqrt{c^2 + 4b\Delta}}{2b}, 0\right), \\ A &= \left(-\frac{c + \sqrt{c^2 + 4b\Delta}}{2b}, 0\right), \\ B/C &= \left(\frac{c}{2b}, \pm \sqrt{\frac{3c^2}{4b^2} - \frac{\Delta}{b}}\right), \end{aligned} \quad (14)$$

with the averaged Fermi velocities

$$\begin{aligned} v_D^2 &= \sqrt{c^2 + 4b\Delta}(2c - \sqrt{c^2 + 4b\Delta}), \\ v_A^2 &= \sqrt{c^2 + 4b\Delta}(2c + \sqrt{c^2 + 4b\Delta}), \\ v_{B/C}^2 &= \sqrt{(5c^2 - 4b\Delta)^2 - 16c^2(c^2 - b\Delta)}. \end{aligned} \quad (15)$$

Moreover, the positions of the saddle points are shifted from those described in Eq. (11) to

$$\begin{aligned} \widehat{AD} &= \left(-\frac{c}{2b}, 0\right) \\ \widehat{BD}/\widehat{CD} &= \left[-\frac{3c^2 + 4b\Delta}{12bc}, \right. \\ &\quad \left. \pm \frac{1}{12bc} \sqrt{(3c^2 - 4b\Delta)(9c^2 + 4b\Delta)}\right]. \end{aligned} \quad (16)$$

The saddle points  $\widehat{BD}$  and  $\widehat{CD}$  are at the same energy:

$$E_{S'} = \frac{1}{12\sqrt{3}bc} (3c^2 - 4b\Delta)^{3/2}, \quad (17)$$

whereas that between  $\widehat{AD}$  is found at

$$E_S = \frac{c^2}{4b} + \Delta \neq E_{S'}. \quad (18)$$

Whenever  $E_S \neq E_{S'}$ , it is possible to define different low-energy regions that make a distinction between the four cones (see Fig. 4). These regions turn out to be useful for the discussion of the LL spectrum in the Sec. III. For instance, in the case  $\Delta < 0$ ,  $E_S < E_{S'}$  and the  $A$  and  $D$  cones start to move closer together and eventually merge when  $E_S = 0$ , that is at  $\Delta = -c^2/4b$ . The other two cones stay apart, well separated [see Fig. 3(a)]. Exactly at the merging transition, the band dispersion is a semi-Dirac one, quadratic in one direction, linear in the other, whereas beyond the transition a gap opens

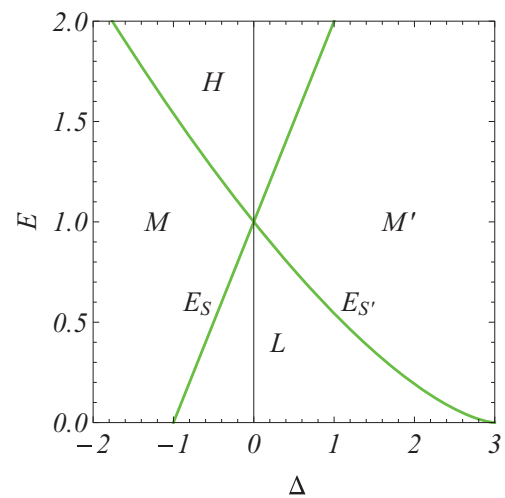


FIG. 4. (Color online) In the plane  $(E, \Delta)$ , the positions of the two saddle points  $E_S$  and  $E_{S'}$  define four distinct regions. The sector  $L$  denotes energies that are below both saddle-point energies  $E_S$  and  $E_{S'}$ , whereas  $H$  describes energies  $E > E_S, E_{S'}$ . The sector  $M$  is defined as energies  $E$ , with  $E_S < E < E_{S'}$ , and  $M'$  for  $E_{S'} < E < E_S$ . Here, the energies are given in units of  $c^2/4b$ .

with a quadratic dispersion in both directions [see Fig. 3(b)]. We emphasize that this merging transition between the pair of Dirac cones is exactly the same as in the case where the two Dirac cones were related by time-reversal symmetry, as discussed in Refs. 22 and 23.

On the other hand, when  $\Delta > 0$  one has  $E_{S'} < E_S$ , such that the  $D$ ,  $B$ , and  $C$  cones converge to a common point whereas  $A$  stands alone. The three cones are coupled at energies around  $E_{S'}$  [see Fig. 3(c)]. At the (triple) merging transition,  $\Delta = 3c^2/4b$ , the crossing bands bear a complex boomerang shape [see Fig. 3(d)], while further increase of  $\Delta$  does not open a gap in the band structure, in contrast to the above-mentioned merging transition for  $\Delta < 0$ . This difference may be understood in terms of winding numbers that play the role of topological charges and that are described in detail in Sec. II D.

Notice that, since trigonal warping is a structure at very low energy ( $\lesssim 10$  meV), a small perturbation is sufficient to drive the system into one of the merging scenarios. For instance, a (triple) merging of the Dirac points occurs at a very small ( $\sim 0.10$  Å) displacement of one graphene layer with respect to the other one, where we use perfect AB stacking as the reference.<sup>15</sup>

### 3. Deformation along an unspecified axis

In addition to the above distortion along a high-symmetry axis of the lattice, we consider the more general deformation along an arbitrary axis that corresponds to a complex-valued  $\Delta$ . Figure 5 shows the evolution of the position of the Dirac points when increasing  $\Delta$  for different values of the angle  $\theta$  defined as  $\Delta = |\Delta|e^{i\theta}$ . The complex position of the merging point in reciprocal space is

$$\pi_m(\theta) = \frac{c}{2b} e^{i\vartheta_m(\theta)}, \quad (19)$$

where the angular dependence of the merging angle  $\vartheta_m(\theta)$  is given by

$$\tan \theta = \frac{2 \sin \vartheta_m - \sin 2\vartheta_m}{\cos 2\vartheta_m + 2 \cos \vartheta_m}, \quad (20)$$

and is plotted in Fig. 6(a). For a given angle  $\theta$ , the merging is reached for a critical value  $\Delta_m(\theta)$  given by

$$\Delta_m(\theta) = \frac{c^2}{4b} [5 + 4 \cos 3\vartheta_m(\theta)]^{1/2}, \quad (21)$$

which is shown in Fig. 6(b).

Equation (20) and Fig. 6(a) reveal that the angular dependence of the merging point,  $\vartheta_m$ , is not linear in the angle of the deformation axis,  $\theta$ . This is best captured in the vicinity of  $\theta = 0$  or  $2\pi/3$  where the slope of the Fig. 6(a) increases abruptly. Most saliently, a slight deviation from a high-symmetry axis ( $\theta = 0, \pm 2\pi/3$ ), i.e., an infinitesimal imaginary contribution to the shift  $\Delta$ , renders the triple-merging point unstable. Indeed, as one may see from Fig. 5, only two Dirac points merge, whereas the third one remains isolated. From this perspective, one can qualify the triple-merging scenario as unstable. However, one can argue that for moderate residual chemical doping or in the presence of disorder, the difference between a triple-merging points and a single-merging point with a close by extra Dirac cone is smeared out, such that the

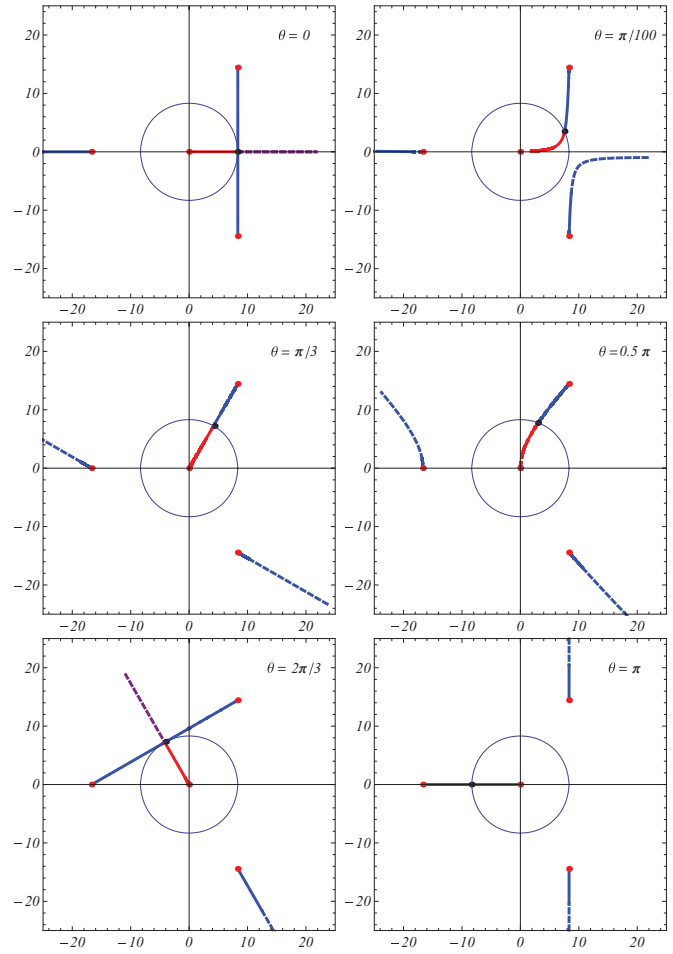


FIG. 5. (Color online) Motion of the Dirac points in momentum space for different values of the displacement angle  $\theta$ . The units are such that  $c = 1$ ,  $b = 0.06$ . When  $\Delta = 0$ , the central Dirac point is surrounded by three Dirac points at distance  $c/b$  (red dots). When increasing  $\Delta$ , the central Dirac point merges with one of the three Dirac points, leaving the two remaining points isolated. When varying  $\theta$ , the position of the merging point draws a circle of radius  $c/2b$ . The full curves represent the positions of the Dirac points until two of them merge. The dashed curves represent the position of the remaining Dirac points after merging of the other two.

study of the triple-merging scenario may still provide physical insight.

### D. Winding numbers

In Sec. II C, we have encountered different merging types of Dirac points that fall into two classes: whereas the merging transition is associated with the opening of a band gap, there are transitions, such as triple merging or those encountered in twisted bilayer graphene,<sup>17</sup> that are not accompanied by a gap opening. The nature of the different merging transitions turns out to be determined by the underlying topological properties of the band Hamiltonian. In this section, we discuss these merging transitions in terms of winding numbers that play the role of topological charges the sum of which is conserved across the transitions. Furthermore, these winding numbers play an eminent role also in the presence of a magnetic

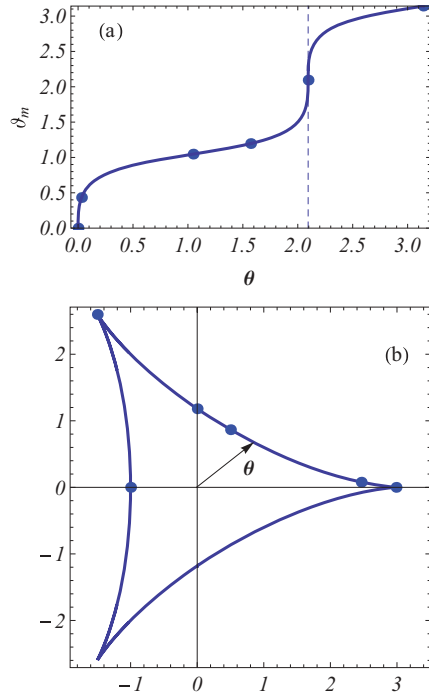


FIG. 6. (Color online) (a) Dependence of the merging position angle  $\vartheta_m$  as a function of the angle of deformation  $\theta$ . The vertical dashed line for  $\theta = 2\pi/3$  indicates the  $2\pi/3$  rotational symmetry. (b) Polar plot of the angular dependence of the critical value  $\Delta_m(\theta)$  of the deformation at the merging.  $\Delta_m$  is given in units of  $c^2/4b$ .

field, where they determine the number of zero-energy modes and where they intervene in the semiclassical treatment that describes to great accuracy the LL spectrum obtained from the full solution of the quantum-mechanical equations (see Sec. IV).

In the vicinity of band-contact points, the system may be described in terms of the effective two-band Hamiltonian

$$\mathcal{H}(\mathbf{q}) = \begin{pmatrix} 0 & h_x(\mathbf{q}) - ih_y(\mathbf{q}) \\ h_x(\mathbf{q}) + ih_y(\mathbf{q}) & 0 \end{pmatrix}, \quad (22)$$

diagonalization of which yields the energy spectrum  $\epsilon_\lambda(\mathbf{q}) = \lambda\sqrt{h_x^2(\mathbf{q}) + h_y^2(\mathbf{q})}$  and the eigenstates

$$\psi = \frac{1}{\sqrt{2}} \begin{pmatrix} 1 \\ \lambda e^{i\phi_{\mathbf{q}}} \end{pmatrix}, \quad (23)$$

where  $\tan \phi_{\mathbf{q}} = h_y(\mathbf{q})/h_x(\mathbf{q})$ , and  $\lambda = \pm 1$  denotes the band index. The relative phase  $\phi_{\mathbf{q}}$  exhibits a particular topological structure that we discuss in terms of the pseudospin map, which is defined as

$$h : \mathbf{q} \longrightarrow \{h_x(\mathbf{q}), h_y(\mathbf{q})\}. \quad (24)$$

Because of the single-valuedness of the wave functions (23), the map  $h = [h_x(\mathbf{q}), h_y(\mathbf{q})]$  must retrieve its original value, modulo  $2\pi$  on a closed path that starts and terminates on a precise value  $\mathbf{q}_0$ . All closed paths therefore fall into distinct homotopy classes that are described by the integer  $w_C$ , which is an element of the homotopy group  $\pi_1(S^1)$  associated with the map  $h$  from the closed path  $\mathcal{C}$  (with the topology of a circle  $S^1$ ) in reciprocal space to closed paths in pseudospin space. In order to calculate this integer, which is the *pseudospin winding*

number, one needs to integrate the Berry connection  $\mathcal{A}_{\mathbf{q}} = i\psi^\dagger \nabla_{\mathbf{q}} \psi$  over the closed path, in terms of the wave functions (23) and the reciprocal-space gradient  $\nabla_{\mathbf{q}} = (\partial/\partial q_x, \partial/\partial q_y)$ . One obtains

$$w(\mathcal{C}) = \frac{1}{2\pi} \oint_{\mathcal{C}} \nabla_{\mathbf{q}} \phi_{\mathbf{q}} \cdot d\mathbf{q}. \quad (25)$$

As such,  $w(\mathcal{C})$  is nothing other than the Berry phase<sup>33,34</sup> within a factor  $\pi$  calculated over the path  $\mathcal{C}$ . However, we avoid the name ‘‘Berry phase’’ in the present context for two reasons. First, the Berry phase does not necessarily need to be an integer, as it has been shown, e.g., in the case of gapped graphene (or boron nitride) where the Berry phase explicitly depends on the energy of the path.<sup>4</sup> Only the topological part, which should then be viewed as the winding number, of this Berry phase determines the chiral properties, such as those revealed by the LL spectrum in the semiclassical approach discussed below. Second, a quantum-mechanical phase is defined modulo  $2\pi$ , and one would therefore not expect different physical properties for  $\pi w_C$  as compared to 0 for even values of  $w_C$  or  $\pi$  for odd values.<sup>35,36</sup> However, relevant properties of the level spectrum, such as the dispersion relation at intermediate energies,<sup>8,35</sup> the degeneracy of the zero-energy modes, and their protection, depend sensitively on the precise value of  $w_C$ . Notice that  $w_C$  is an additive quantity—if one divides the surface  $\Sigma$  enclosed by the path  $\mathcal{C}$  into distinct pieces,  $\Sigma_1, \dots, \Sigma_N$ , the winding number is the sum of the partial ones calculated over paths  $\mathcal{C}_j$  encircling the surfaces  $\Sigma_j$ ,

$$w(\mathcal{C}) = \sum_{j=1}^N w(\mathcal{C}_j). \quad (26)$$

Furthermore, if one of the merging transitions discussed in Sec. II C takes place inside a path  $\mathcal{C}$ , the winding number is a conserved quantity. It is simply the sum of the winding numbers calculated on paths around the original band-contact points before the merging transition and may thus also be viewed as a topological charge.

As an example, we plot the map (24) in Fig. 7 for the Hamiltonian  $\mathcal{H}_b + \mathcal{H}_c + \mathcal{H}_\Delta$  in different configurations corresponding to the sectors L, H, M, and M’ of Fig. 4. In the low-energy sector (L), for energies below both saddle points  $E_S$  and  $E_{S'}$ , all Dirac points are resolved, and there exist thus closed loops encircling each of the points [see Fig. 7(a)]. The vicinity of the points A, B, and C is then described by a charge +1 each, whereas the central point D carries a charge  $-1$ . At energies larger than  $E_S$  and  $E_{S'}$  [sector H, Fig. 7(b)], all closed loops necessarily enclose all points, and the topological charge is therefore the sum (+2) of all individual Dirac points resolved at low energies. This situation is to be contrasted to the sector M, for energies  $E$  with  $E_S < E < E_{S'}$ , [see Fig. 7(c)]. The points A and D are then necessarily enclosed by all corresponding loops, such that the charge is 0, whereas a second class of loops can still resolve the points B and C (charge +1 each). In the sector M’, for  $E_{S'} < E < E_S$ , the three points B, C, and D can no longer be resolved (loops of charge +1), whereas A remains a Dirac point with charge +1 [see Fig. 7(d)].

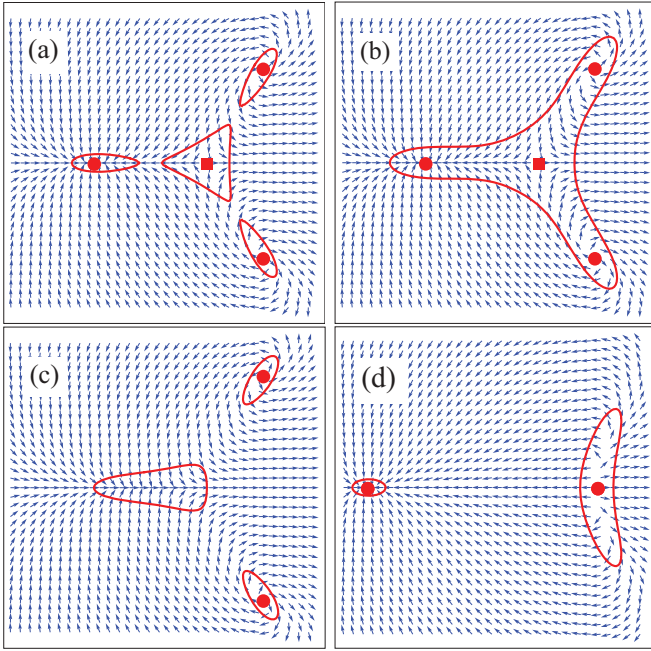


FIG. 7. (Color online) Winding numbers for the pseudospin map. The square indicates a charge  $-1$  and the circles indicate a charge  $+1$ . (a) In the sector L, all Dirac points are resolved and described by individual topological charges. (b) Sector H, the possible closed loops enclose all Dirac points, and the topological charge is thus 2. (c) Sector M, whereas the Dirac points B and C are resolved (charge 1), the points A and D have merged, such that closed loops yield a charge 0. (d) Sector  $M'$ , the triple merging involves the points B, C, and D and closed loops yield a charge 1, in addition to the charge 1 stemming from the isolated Dirac point A.

In view of the different merging transitions, we have already mentioned that the pseudospin winding number is conserved during such transitions. For merging ( $\Delta < 0$ ) of two Dirac points described by winding numbers of opposite sign (e.g.,  $w_D = -1$  and  $w_A = +1$ )—this is necessarily the case for Dirac points that are related by time-reversal symmetry—the topological charges are thus annihilated across the transition, such that the zero-energy states are no longer topologically protected. One therefore observes the opening of a local band gap that is associated with the merging of Dirac points with opposite winding numbers [see Figs. 3(a) and 3(b)]. In the case of a triple merging ( $\Delta > 0$ ), the sum of the winding numbers is  $w_B + w_C + w_D = +1$ , such that any path enclosing the point where the Dirac points B, C, and D have merged carries a winding number  $+1$  also after the transition. The (zero-energy) band contact is therefore preserved and the opening of a band gap topologically prohibited [see Figs. 3(c) and 3(d)].

### III. LANDAU LEVEL SPECTRUM

The considerations of the previous section on the band structure in the absence of a magnetic field yield valuable insight into the LL spectrum, which is formed when a perpendicular magnetic field,  $B\mathbf{e}_z = \nabla \times \mathbf{A}$ , is applied to the graphene layers. In this section, we compare the LL spectrum obtained from a numerical solution of the full quantum-mechanical problem described by the Hamiltonian  $\mathcal{H}_b + \mathcal{H}_c +$

$\mathcal{H}_\Delta$  in the presence of a magnetic field (see Sec. III A) to that calculated within a semiclassical approximation (see Sec. III B). A detailed discussion of the LLs in the different energy sectors (L, M,  $M'$ , and H) is postponed to Sec. V.

#### A. Landau quantization

The magnetic field may be taken into account with the help of the Peierls substitution (for electrons of charge  $-e$ )

$$\Pi = \pi + e\mathbf{A}, \quad (27)$$

where  $\mathbf{A}$  is the vector potential. This allows one to introduce the harmonic oscillator operators

$$a = \frac{l_B}{\sqrt{2}}(\Pi_x - i\Pi_y), \quad a^\dagger = \frac{l_B}{\sqrt{2}}(\Pi_x + i\Pi_y), \quad (28)$$

with  $[a, a^\dagger] = 1$ . The magnetic length  $l_B = 1/\sqrt{eB} \simeq 26 \text{ nm}/\sqrt{B[\text{T}]}$  encodes the size of the cyclotron orbits in real space.

In the presence of a magnetic field, the Hamiltonian  $\mathcal{H}_b + \mathcal{H}_c + \mathcal{H}_\Delta$  reads

$$\frac{\mathcal{H}_B}{c/l_B} = \begin{pmatrix} 0 & 2\beta a^2 - \sqrt{2}a^\dagger - \delta \\ 2\beta a^{\dagger 2} - \sqrt{2}a - \delta & 0 \end{pmatrix}. \quad (29)$$

We have rescaled the energy with respect to  $c/l_B = c\sqrt{eB}$ , the characteristic LL energy of the central Dirac cone  $D$  for  $\delta = 0$ , and have also introduced the dimensionless ( $B$ -field-dependent) shift  $\delta = \Delta/c\sqrt{eB}$  as well as the parameter

$$\beta = \frac{b\sqrt{eB}}{c}. \quad (30)$$

The quantity  $\beta$ , which measures the amplitude of the trigonal warping in units of the inverse magnetic length, is a central parameter in the description of the LL spectrum. It may also be interpreted as the inverse of the reciprocal-space distance  $c/b$  of a peripheral Dirac cone ( $A, B, C$ ) to the central one ( $D$ ) and the magnetic length  $l_B$ . Viewed as an energy scale, it is proportional to the ratio between the first excited LL ( $c\sqrt{2eB}$ ) and the energy  $E_S$  of the saddle points joining the cones [in the absence of a deformation (at  $\delta = 0$ )]. From Eq. (12), we have

$$\frac{c\sqrt{2eB}}{E_S} = 4\sqrt{2}\beta. \quad (31)$$

Finally, the parameter  $\beta$  turns out to describe the role of magnetic blurring that is described in Sec. IV B. Notice that one might also have performed the Peierls substitution in the original four-band model (1), as it has been done for the case without trigonal warping.<sup>37</sup> However, the corrections are weak in the low-energy limit that we are interested in, and the effective two-band model (29) provides a good description of the LL spectrum.

The numerically obtained spectrum of Hamiltonian (29) is plotted in Fig. 8 as a function of  $\delta$ , which corresponds to varying  $\Delta$  and/or  $B$  as well as the energy of the saddle points in order to sustain the same number of LL below  $E_S$ . Notice that we have only plotted the spectrum at positive energy,  $\epsilon_n$ , those at negative energy are obtained from the plotted ones simply by adding a minus sign,  $-\epsilon_n$ , as a consequence of the particle-hole symmetry respected by Hamiltonian (29). Increasing the value

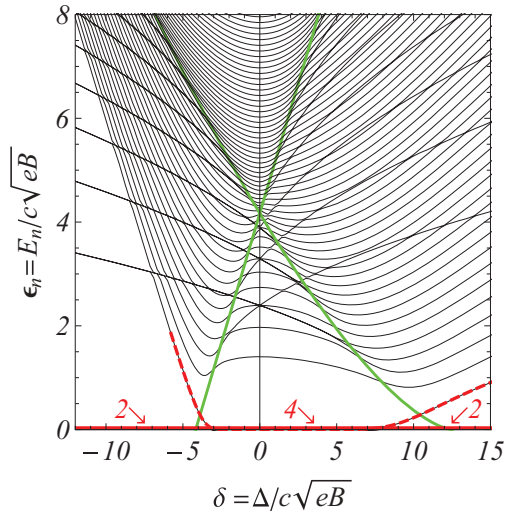


FIG. 8. (Color online) LL spectrum of the Hamiltonian (29) as a function of  $\delta$ . The parameter  $\beta$  is fixed to 0.06. The spectrum is cut into four parts delimited by the thick (green) lines that depict the energy of the saddle points in units of  $c/l_B = c\sqrt{eB}$ . The figure shows the existence of four zero-energy modes. Two of them (red) are topologically stable. The other two (here only the one of positive energy is marked with a dashed curve) acquire a finite energy for sufficiently large values of  $\delta$ .

of  $\beta$  will then only scroll the levels up in energy and reduce the number of modes within the trigonally warped area. For this reason, we focus on an arbitrarily low value of  $\beta = 0.06$ . The spectra for other values of  $\beta$  are discussed in Sec. IV B.

### B. Semiclassical description

In order to reproduce the spectrum of Fig. 8 and to understand the underlying physical properties, we rely on a semiclassical analysis. This theory states, according to Onsager's argument,<sup>38,39</sup> that the reciprocal-space area  $\mathcal{A}_C(\epsilon_n)$  enclosed by the band contour  $\mathcal{C}$ , for energy  $\epsilon_n$ , must fulfill

$$\mathcal{A}_C(\epsilon_n) = \int_{\mathbf{k}(\epsilon \leq \epsilon_n)} d^2k = 2\pi eB(n + \gamma), \quad (32)$$

where the mismatch factor

$$\gamma = \frac{1}{2} - \gamma_B \quad (33)$$

has a contribution 1/2 from the usual Maslov index for the harmonic oscillator and a second one,  $\gamma_B$ , that was first identified with the Berry phase<sup>40,41</sup> acquired on the path  $\mathcal{C}$ , whereas it has been shown afterwards that only the topological part of the Berry phase enters into the expression.<sup>4</sup> Here, we express the quantity  $\gamma_B$  in terms of the pseudospin winding number,  $\gamma_B = |w_C|/2$ , such that Eq. (33) becomes<sup>27</sup>

$$\gamma = \frac{1}{2} - \frac{|w_C|}{2}. \quad (34)$$

At first sight, the large- $n$  limit of the semiclassical approximation could be described in terms of a quantum-mechanical Berry phase  $\pi|w_C|$  modulo  $2\pi$ , that is one identifies all odd and all even winding numbers, if one redefines the integer  $n$ . However, Eq. (34) bears information about the presence and the number of zero-energy modes [see Sec. IV].

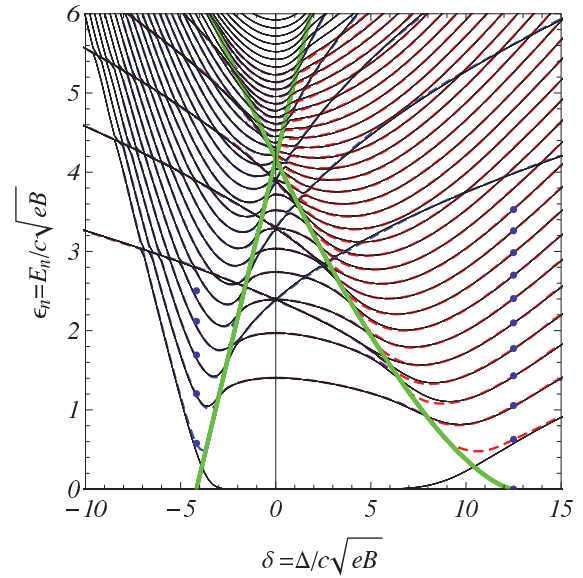


FIG. 9. (Color online) Semiclassical reconstruction (dashed lines) of the spectrum in Fig. 8, for  $\beta = 0.06$ . The different regions of the spectrum are discussed in detail in Sec. V. The blue dots indicate the LL spectrum at the merging (left) and the triple-merging transition (right), in which case the LLs scale as  $(n + 1/2)^{2/3}$  and  $n^{3/4}$ , respectively, see Secs. V C and V D. The green lines indicate the energies of the saddle points  $\epsilon_S$  and  $\epsilon_{S'}$ .

In order to obtain the semiclassical LL spectrum  $\epsilon_n = \epsilon(n)$ , we numerically invert Eq. (32). The results are shown in Fig. 9 (dashed lines) in comparison with the ones (full lines) obtained from a numerical solution of the quantum-mechanical eigenvalue equation [Hamiltonian (29)].

In addition to the LL spectrum, Figs. 8 and 9 depict the energy of the saddle points rescaled by the energy  $c/l_B$  (thick green lines),

$$\epsilon_S = E_S/c\sqrt{eB}, \quad \epsilon_{S'} = E_{S'}/c\sqrt{eB}. \quad (35)$$

Whenever a LL crosses one of the three saddle points, its properties, such as its degeneracy, are drastically modified due to the Lifshitz transition involved. Indeed, Figs. 8 and 9 reveal four distinct sectors L, H, M, and M' introduced in Fig. 4 according to whether the energy is below both saddle points [low-energy sector (L)], below only one of the saddle points [merging (M) and triple-merging (M') sectors], or above both of them for the high-energy sector (H) [see Fig. 14(a)]. For these distinct regions, Onsager's quantization reads differently, because the winding number  $w_C$  takes different values for different types of orbits. The different sectors are shown on Fig. 10 and discussed in detail in Sec. V.

## IV. ZERO MODES AND SEMICLASSICAL QUANTIZATION RULE

In principle, the semiclassical description is valid at large energies, whereas the zero modes require a specific (quantum-mechanical) treatment. However, the semiclassical analysis and the intervening winding numbers provide valuable insight into the degeneracy of the zero modes. The discussion of this relation is the issue of the present section. In Sec. IV A, we

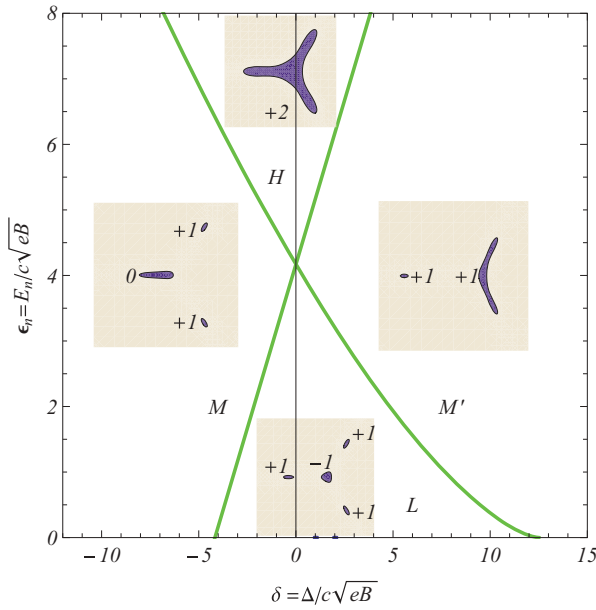


FIG. 10. (Color online) The different winding numbers attached to the different pockets imply different quantization rules.

provide a simplified model to illustrate this relation, whereas we discuss the LL degeneracy lifting due to magnetic blurring in Sec. IV B.

#### A. Relation between zero modes and winding number

We provide here a heuristic argument relating the total number of topologically protected zero-energy modes to the semiclassical quantization rule. Consider first the model Hamiltonian<sup>27,31,42</sup>

$$\mathcal{H} = \Lambda \begin{pmatrix} 0 & \pi^{\dagger p} \\ \pi^p & 0 \end{pmatrix} \quad (36)$$

describing a band contact point with energy spectrum  $\epsilon = \pm \Lambda |\mathbf{q}|^p$  and with a winding number  $p$ . The global parameter  $\Lambda$  has the physical dimension of an energy times the  $p$ th power of a length. In a magnetic field, performing the Peierls substitution (27) and the replacement in terms of ladder operators (28), one obtains the LL spectrum in a magnetic field,

$$\epsilon_n(B) = \pm \Lambda (2eB)^{p/2} \sqrt{n(n-1) \cdots (n-p+1)}, \quad (37)$$

which in the large- $n$  limit, may be approximated as

$$\epsilon_n(B) \simeq \pm \Lambda \left[ 2eB \left( n + \frac{1}{2} - \frac{p}{2} \right) \right]^{p/2}. \quad (38)$$

This corresponds precisely to the semiclassical quantization rule (32) if we identify  $p$  with the total winding number  $w_C$  in Eq. (34). From Eq. (37), one notices that the  $p$  quantum numbers  $n = 0, \dots, p-1$  correspond to states at zero energy. Indeed, these states may be obtained from the eigenvalue equation

$$\mathcal{H} \begin{pmatrix} u_n \\ v_n \end{pmatrix} = 0, \quad (39)$$

which is satisfied for the states

$$\psi_n^{(0)} = \begin{pmatrix} 0 \\ |n\rangle \end{pmatrix}, \quad \text{for } n = 0, \dots, p-1 \quad (40)$$

in terms of the eigenstates  $|n\rangle$  of the number operator  $a^\dagger a$ ,  $a^\dagger a |n\rangle = n |n\rangle$ . Because of the orthogonality of the states, the zero-energy manifold is  $p$ -fold degenerate, i.e., the degeneracy corresponds to the total winding number  $w_C = p$ , as stated above.

The situation is different when there are more band-contact points, with different (local) winding numbers. Consider a Hamiltonian describing  $p$  massless Dirac points with winding number  $+1$ , situated at the complex positions  $\alpha_i$  in reciprocal space, and  $p'$  massless Dirac points with winding number  $-1$ , at the positions  $\beta_j$ . (Notice that band contact points with larger winding numbers may be obtained by making several positions  $\alpha_i$  or  $\beta_j$  coincide.) The Hamiltonian can be written as

$$\mathcal{H}_q = \Lambda \begin{pmatrix} 0 & f_q \\ f_q^* & 0 \end{pmatrix}, \quad (41)$$

with  $f_q = \prod_{j=1}^{p'} (\pi^\dagger - \beta_j^*) \prod_{i=1}^p (\pi - \alpha_i)$  and  $\Lambda$  is a global constant of the dimension energy times the  $(p+p')$ -th power of a length. The total number of Dirac points, and thus, after the Peierls substitution (27), the maximal number of zero-energy LL, is  $w_t = p + p'$ . However, this  $(p+p')$ -fold degeneracy of the zero modes may be partially lifted upon merging of two or more Dirac points. In order to find the total number of topologically protected zero-energy levels, we thus continuously modify the parameters

$$\alpha_i \rightarrow 0 \quad \text{and} \quad \beta_j \rightarrow 0, \quad (42)$$

so that  $f_q$  becomes  $\pi^{\dagger p'} \pi^p$ . In a magnetic field, assuming for example that  $p > p'$ , this term is of the form  $\sqrt{2eB}^{w_t} (a^\dagger a)^{p'} a^{p-p'}$ , and the associated LL spectrum reads

$$\epsilon_n(B) = \pm \Lambda (2eB)^{w_t/2} n^{p'} \sqrt{n(n-1) \cdots (n-p+p'+1)}. \quad (43)$$

The same arguments as those presented in the discussion of the Hamiltonian (36) indicate that there are  $w_p = p - p'$  zero-energy levels that correspond to the quantum numbers  $n = 0, \dots, p - p' - 1$ . Moreover, the same large- $n$  expansion as in the case discussed above yields the spectrum

$$\epsilon_n(B) \simeq \pm \Lambda (2eB)^{\frac{p+p'}{2}} n^{p'} \left( n + \frac{1}{2} - \frac{w_p}{2} \right)^{w_p/2}, \quad (44)$$

which may be cast into the semiclassical quantization rule with a winding number  $w_C = w_p = p - p'$ . Again the total winding number is identical to the number of zero-energy modes.

These arguments show that, although the maximum number of zero-energy LLs is  $w_t = p + p'$ , a quantum-mechanical coupling between them partially lifts the degeneracy, but  $w_p = |p - p'|$  zero modes remain topologically protected. Applied to the model (8), one has  $p = 3$  and  $p' = 1$ , so that the maximal number of zero modes is  $w_t = 4$  and the number of topologically protected modes is  $w_p = 2$ .

### B. Magnetic blurring

It is apparent from Fig. 9 that the semiclassical treatment (32) based on Onsager's quantization rule provides a reliable description of the LL spectrum in the major part of the parameter range. However, it is challenged in the vicinity of the saddle points  $\epsilon_S$  and  $\epsilon_{S'}$ . Intuitively, one may understand the failure of semiclassical quantization if one considers the topological winding number (25) that is calculated from closed loops around the remarkable points in reciprocal space [see Fig. 7]—in the presence of a strong magnetic field, these loops are at odds with quantum mechanics because the components of the wave vector are no longer good quantum numbers, such that the images of the loops defined by the maps (24) are constrained by a Heisenberg uncertainty relation.

Indeed, in the presence of a magnetic field, the momenta no longer verify the simple commutation relation  $[\Pi_x, \Pi_y] = 0$  but rather a Heisenberg algebra

$$[\Pi_x, \Pi_y] = -\frac{i}{l_B^2}. \quad (45)$$

An immediate consequence of this non-commutative geometry is that reciprocal space is now “patched” or “blurred” by irreducible regions of area  $1/l_B^2$  below which it is impossible to resolve the physical properties of electrons in a magnetic field. This is similar to the phase space of a one-dimensional quantum-mechanical particle, which is divided into minimal regions of the size of the Planck constant  $h = 2\pi$ , below which the physical properties of the particle cannot be resolved. As a consequence, the winding of the pseudospin vector cannot be determined by paths the area of which encloses less than the minimal area of  $\propto 1/l_B^2$ , which plays the role of the Planck constant in reciprocal space. If we were to define a winding number in the noncommutative reciprocal space, we should then consider larger and larger contours as the magnetic field increases since  $1/l_B^2 \propto B$ , as shown in Fig. 11.

One may thus pictorially understand that whenever the irreducible area of  $1/l_B^2$  becomes too large, the relevant winding contours enclose inevitably more than one singularity.

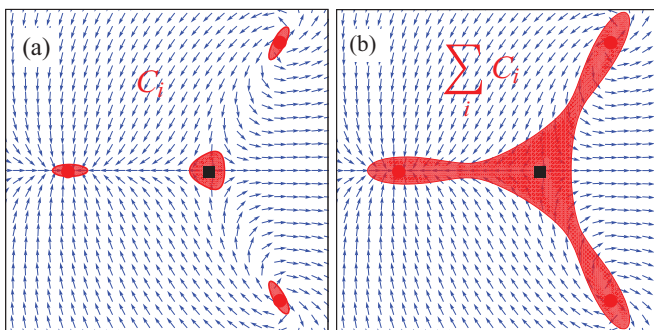


FIG. 11. (Color online) Magnetic blurring for zero modes. Each contour encloses a minimal surface of  $\sim 1/l_B^2 = eB$  in reciprocal space (red areas). (a) At low magnetic fields, the blurring is low, and each minimal surface contains a single Dirac point. The semiclassical quantization rule holds for each contour encircling a Dirac point. (b) When the field increases, the contour associated with the zero mode encloses a larger surface so that the individual Dirac points are no longer resolved. The effective winding number experienced by the electron is  $w_p = \sum_i w_i$ .

This is shown in Fig. 11 where at low fields the contours  $C_i$  around the individual singularities enclose each a winding number  $w_i = \pm 1$ , whereas at high fields the blurred contour encloses a winding number  $\sum_i w_i = 2$ . Therefore, for a sufficiently strong magnetic field, the only relevant quantity is the total winding number around *all* the singularities,

$$w_p = \left| \sum_i w_i \right|, \quad (46)$$

as opposed to the total sum of the winding numbers,

$$w_t = \sum_i |w_i|, \quad (47)$$

which sets the total number (but not necessarily protected) of Dirac points. In the model Hamiltonian discussed in Sec. IV A, this magnetic blurring may be viewed alternatively as an effective merging of the band-contact points (42).

As a consequence of the above arguments, increasing the magnetic field induces, even at zero energy, a Lifshitz transition that is characterized by a partial degeneracy lifting of the zero-energy LL from  $w_t$  (per spin and valley) to  $w_p \leq w_t$ , while  $w_t - w_p$  levels disperse as a function of  $B$ .

In the case of the Hamiltonian (29), we generally have four Dirac points in the vicinity of  $\delta = 0$  such that one expects a

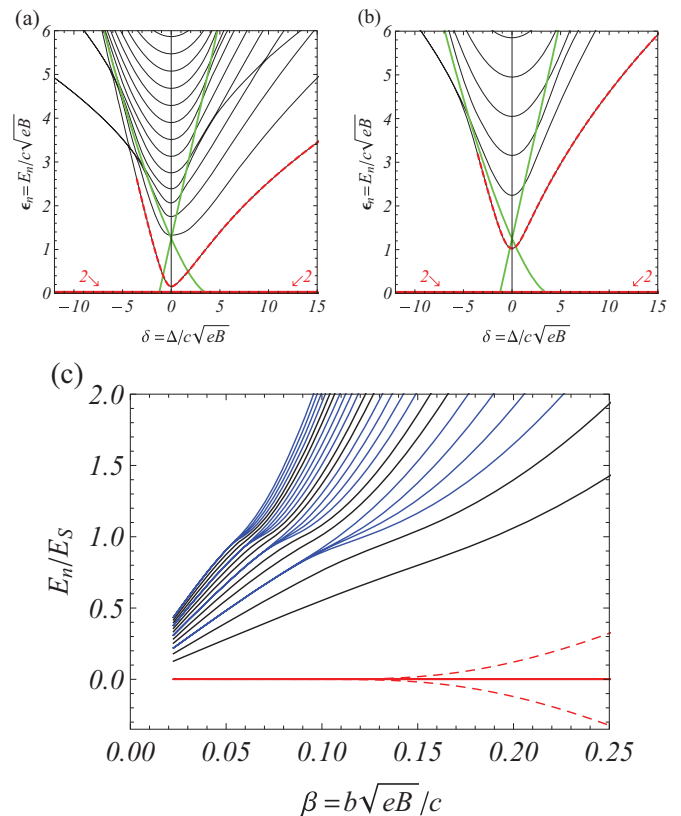


FIG. 12. (Color online) LL spectrum of the Hamiltonian (29) as a function of  $\delta$ . The parameter  $\beta$  is fixed to 0.2 (a) and 0.45 (b). (c) LLs as a function of the parameter  $\beta$  in the absence of distortion ( $\delta = 0$ ). It exhibits the lift of the fourfold degeneracy when the energy of the LLs becomes larger than the saddle point energy  $E_S$  (blue levels). Two zero-energy levels stay stable, while two other levels get a finite energy when  $\beta \gtrsim 1/4\sqrt{2} \simeq 0.18$ .

fourfold degeneracy of the zero-energy mode for low magnetic fields, in agreement with Eq. (46). Because of the parameter  $\beta \propto \sqrt{B}$  [see Eq. (30)], the low-field limit corresponds to small values of  $\beta$ , such as in the case of the value 0.06 chosen to calculate the spectrum in Figs. 8 and 9. Indeed, the fourfold degeneracy of the zero mode is lifted only when approaching the merging transitions from 4 to 2, where  $\beta$  diverges as a consequence of the decreasing reciprocal-space distance between some of the Dirac points. However, this degeneracy can also be lifted exactly at  $\delta = 0$  by increasing the value of  $\beta$ , where Fig. 11 and Eq. (47) indicate that the degeneracy of the zero-energy mode is 2 above a certain magnetic field. The quantum-mechanical LL spectra, for larger values of  $\beta$ , are depicted in Fig. 12(a) for  $\beta = 0.2$  and for 0.45 in Fig. 12(b), as a function of  $\delta$ . In both cases, one notices that the fourfold degeneracy is indeed lifted for all values of  $\delta$ , in agreement with the expectation from magnetic blurring. The effect is also apparent in Fig. 12(c), where we have plotted the  $\delta = 0$  LL spectrum in units of the saddle-point energy  $E_S$  as a function of  $\beta$ . Indeed two branches of the small- $\beta$  zero-energy mode float away—due to particle-hole symmetry, one increases in energy while the other one decreases—while two other branches are topologically protected and remain at zero energy.

Notice that the magnetic blurring in reciprocal space may also be understood as a blurring in energy. Indeed, the commutation relations (45) induce, via the maps (24), commutation relations for the pseudospin components that read, to lowest order in  $l_B^2$ ,

$$[h_x, h_y] \simeq \frac{i}{l_B^2} \left( \frac{\partial h_x}{\partial \Pi_y} \frac{\partial h_y}{\partial \Pi_x} - \frac{\partial h_x}{\partial \Pi_x} \frac{\partial h_y}{\partial \Pi_y} \right). \quad (48)$$

In the vicinity of a Dirac point  $j$  with linear band dispersion and a characteristic (possibly anisotropic) Fermi velocity  $(v_{x,j}, v_{y,j})$ , the commutation relations (48) thus induce a Heisenberg uncertainty relation  $\Delta h_x \Delta h_y \sim v_{x,j} v_{y,j} / l_B^2 = v_j^2 / l_B^2$  that is precisely on the order of the energy gap between the zero-energy level and the first excited one. In this picture, the topological winding numbers and thus the level degeneracies associated with individual contours around the Dirac points are well defined as long as the energy uncertainty  $\sqrt{\Delta h_x \Delta h_y} \sim v_j / l_B$  is smaller than the saddle point  $E_S$ . This argument agrees with the expectation that the zero-mode degeneracy is lifted once

$$E_S \lesssim \sqrt{2} c \sqrt{eB} \Leftrightarrow \beta \gtrsim \frac{1}{4\sqrt{2}}, \quad (49)$$

In addition to the zero-energy modes, magnetic blurring also plays a role in the degeneracy lifting of higher-energy LLs in the vicinity of the saddle points, where the semiclassical approximation does not accurately describe the LL spectrum [see Fig. 9]. Indeed, the degeneracy lifting in the semiclassical approximation is abrupt because of the abrupt change in the winding number: for energies just below the saddle points, one has disconnected energy contours  $C$  and  $C'$  that become connected by a contour  $C + C'$  for infinitesimal energies above the saddle points. However, this abrupt transition is blurred because not only the above-mentioned smallest contours, which are responsible for zero-energy modes, need to enclose a minimal surface of  $\sim 1/l_B^2$ , but also two contours

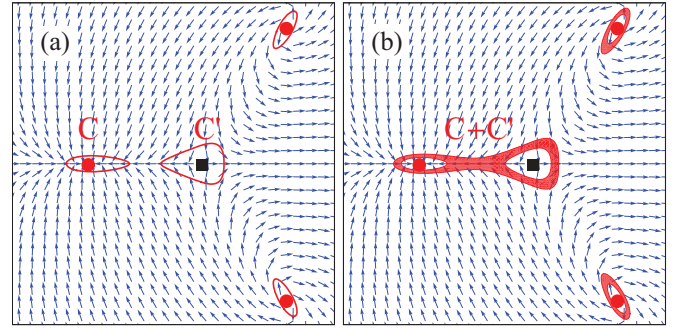


FIG. 13. (Color online) Magnetic blurring for contours at higher energy. (a) At low magnetic fields, the semiclassical quantization rule holds for each contour encircling a Dirac point. (b) When the field increases, the energy contours become blurred and tunneling to trajectories enclosing two singularities becomes possible in the vicinity of the saddle points. The effective number experienced by the electron is  $w_{(C+C')} = w_C + w_{C'} = 0$  for the upper bound of the contour, whereas it is  $|w_C| + |w_{C'}| = 2$  for the lower bound.

corresponding to successive energy levels (see Fig. 13). The resulting uncertainty about whether a contour in the red region in Fig. 13 is connected or disconnected yields an uncertainty in the winding number, such that the variation of the LLs in the vicinity of saddle points is smoother than that expected from the semiclassical analysis.

## V. DETAILED ANALYSIS OF THE SPECTRUM

The semiclassical and topological theories presented in Secs. III B and IV, respectively, allow us to discuss in detail the different properties of the LL spectrum in Fig. 8. From the semiclassical quantization (32) with appropriate values of the winding number  $w_C$ , we obtain the semiclassical spectrum in the different energy regions separated by the saddle-point energies. Unless stated explicitly, we discuss only the orbital degeneracy for a single valley ( $K$  or  $K'$ ) and a single spin—the full degeneracy is then given by the orbital degeneracy times the fourfold spin-valley degeneracy.

### A. Undistorted Case $\delta = 0$

We begin our reconstruction of the spectrum by plotting the LL at  $\delta = 0$  ( $\Delta = 0$ ), that is without any distortion, see vertical lines in Figs. 14(a) and 14(b). As long as the energy satisfies  $\epsilon < \epsilon_S = \epsilon_{S'}$ , the LLs lie in the central region of the low-energy sector (L), see Fig. 14(a). In the absence of a magnetic field, the low-energy spectrum is that of Fig. 2(a) and consists of four Dirac cones,  $A$  to  $D$ . The four Dirac cones give rise to four disconnected Fermi pockets the area of which is

$$\mathcal{A}_0 = \pi \frac{\epsilon^2}{c^2} \quad \mathcal{A}_p = \pi \frac{\epsilon^2}{3c^2}, \quad (50)$$

where  $\mathcal{A}_0$  is the area of the central cone ( $D$ ) and  $\mathcal{A}_p$  that of the other peripheral ones. In the vicinity of each isolated Dirac cone, one has a topological charge of  $w_C = \pm 1$ , as in the case of monolayer graphene, such that Onsager's quantization rule

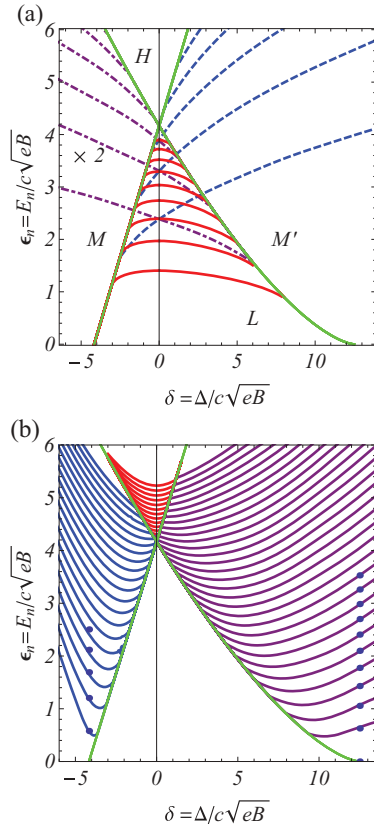


FIG. 14. (Color online) Different sectors of the LL spectrum, for  $\beta = 0.06$ . (a) Landau levels in the low-energy sector (L) obtained from the semiclassical approximation  $\mathcal{A} = 2\pi eBn$ . The red levels correspond to the quantization of the  $D$  cone, the blue dashed levels to the quantization of the  $A$  cone. The last set (purple dashed-dotted) of levels is twofold degenerate since it corresponds to the quantization of the two cones labeled  $B$  and  $C$ . (b) Landau levels in the high-energy sector (above the saddle points). The blue levels in the  $M$  region are obtained from the semiclassical approximation  $\mathcal{A} = 2\pi eB(n + 1/2)$  corresponding to the absence of winding number. The purple levels in the  $M'$  zone are obtained from the condition  $\mathcal{A} = 2\pi eBn$  of the pocket issued from the  $B, C, D$  cones. The blue dots indicate the LL spectrum at the merging (left) and the triple-merging transition (right), in which case the LLs scale as  $(n + 1/2)^{2/3}$  and  $n^{3/4}$ , respectively. In the high-energy region  $H$ , the four Dirac pockets have merged into a single pocket with a total winding number 2, so that the red levels are obtained from the condition  $\mathcal{A} = 2\pi eB(n + 1/2)$ .

(32) yields

$$2\pi \left( n + \frac{1}{2} - \frac{|wc|}{2} \right) eB = 2\pi neB = \mathcal{A}(E)$$

$$\Rightarrow E_0(n) = c\sqrt{2neB}, \quad E_p(n) = c\sqrt{6neB}. \quad (51)$$

At zero energy and for moderate magnetic fields ( $\beta = b\sqrt{eB}/c \ll 1$ , as in Fig. 8), one thus obtains a fourfold orbital degeneracy of the zero-energy level because each of the four Dirac cones yields an  $n = 0$  LL. Therefore the total degeneracy of the zero-energy level, taking into account again the additional fourfold spin-valley degeneracy, is 16. From the topological point of view, this is related to the presence of four well-separated Dirac points that are not yet blurred by the relatively moderate magnetic field,  $\beta \ll 1$ , in such a manner

that the four related winding numbers are decoupled and give rise to four zero-energy LLs.

For higher (relativistic) LL, we find three times more LLs for the central cone because  $\mathcal{A}_0 = 3\mathcal{A}_p$ . This explains the fourfold degeneracy displayed one time out of three in Fig. 14(a). Indeed, every third LL is not only associated with the central Dirac point but also with the three peripheral ones; hence its (accidental) fourfold orbital degeneracy, whereas the other LLs are nondegenerate because they are associated with the central one only. As we have previously discussed [see Eq. (10)], the averaged Fermi velocity at the points  $A$ ,  $B$ , and  $C$  is  $\sqrt{3}$  times larger than that,  $c$ , around the  $D$  point,  $v_A = v_{B/C} = \sqrt{3}v_D$ . The three times denser LL spectrum associated with the central cone is therefore a consequence of this relation between the Fermi velocities and of the approximate LL dispersion

$$E_{\pm,n} = \pm \frac{v_j}{l_B} \sqrt{2n} \quad (52)$$

around the Dirac points, with their typical  $\sqrt{n}$  scaling, for  $j = A, B, C$ , or  $D$ .

Crossing the transition lines at  $\epsilon = \epsilon_S = \epsilon_{S'}$ , the spectrum undergoes a transition to the high-energy sector (H), see Fig. 14(b). At zero magnetic field, the three peripheral Fermi pockets merge with the central one. This change in the topology of the Fermi surface has consequences for the degeneracy, in the sense that Onsager's quantization rule indicates that there is only one set of LLs associated with the simply connected Fermi surface. There is thus no more orbital LL degeneracy and, besides the trigonal deformation of the Fermi surface, the band structure is approximately parabolic such that the LLs scale as  $n$ , as in the usual description of Bernal-stacked bilayer graphene [ $\sqrt{n(n-1)} \sim n - 1/2$ ].

### B. Slightly distorted case $0 < |\delta| \ll 1$

For small nonzero values of the parameter  $\delta$ , the saddle points occur at two different energies,  $\epsilon_S \neq \epsilon_{S'}$ , and one therefore needs to distinguish three different energy sectors, that is L, M, and H for  $\delta < 0$  and L, M', and H for  $\delta > 0$  [see Fig. 10]. Below the energies  $\epsilon_S$  and  $\epsilon_{S'}$ , the band structure is that of Figs. 3(b) or 3(e), comprising four Dirac cones albeit with no trigonal symmetry due to finite distortion of the bilayer. For small values of  $\beta$ , the picture obtained in the discussion of the  $\delta = 0$  case remains essentially unaltered at zero energy. The presence of four distinguishable Dirac cones yields a fourfold zero-energy level that is insensitive to the slight geometric deformation of the perfectly trigonally warped case. As a consequence, the zero modes remain untouched over a wide range of  $\delta$  distortion around 0.

On the other hand, the higher LL are not topologically protected and the breaking of the trigonal symmetry induces an immediate lift of orbital degeneracy, as pictured in Fig. 14. Our choice of a real valued parameter  $\Delta$  implies that the Dirac cones  $B$  and  $C$  are related by mirror symmetry, such that  $v_B = v_C$ . The corresponding LLs [thick blue lines in Fig. 14(a)] are therefore twofold degenerate and experience the strongest decrease in energy with increasing  $\delta > 0$  because their average Fermi velocity is decreased [see Eq. (15)]. The other two sublevels have a single orbital degeneracy,

corresponding to the Dirac cones  $A$  and  $D$ . As one may see from Eq. (15), the Fermi velocity of the central cone  $D$  decreases (quadratically in  $\delta$ ), whereas that of the cone  $A$  increases linearly in  $\delta$ . As a consequence, the energy of the LLs associated with  $D$  [red lines in Fig. 14(a)] is decreased both for positive and negative values of  $\delta$ , whereas the  $A$ -cone LLs increase linearly in energy with increasing  $\delta$ . Above both saddle points, i.e., in the sector H, varying  $\delta$  always yields a decrease in the size of the unique Fermi surface so that the non-degenerate LL are enhanced in energy, as one may see in Fig. 14(b).

### C. Merging transition $\delta \ll -1$

In Sec. IV B, we have shown that the fate of the zero-energy level is determined by the parameter  $\beta$ ; upon increase of  $\beta$ , one obtains a magnetic-field-induced Lifshitz transition from a fourfold degenerate to a twofold degenerate level. Whereas this picture is roughly the same for small values of  $|\delta|$ , it needs to be modified when approaching the zero-field merging transition, that is when the saddle point energy  $\epsilon_S$  vanishes. As one may see from Fig. 8, one notices a significant departure from the semiclassical approximation. The  $A$  and  $D$  Fermi pockets merge indeed into a single one and the corresponding orbital degeneracy of the LLs is changed. Indeed, because of the decrease in energy of the saddle point  $E_S$ , the latter is only higher in energy than the typical scale  $\sqrt{2}c\sqrt{eB}$  for the separation between the lowest LLs if

$$1 \lesssim \frac{1}{4\sqrt{2}\beta} + \frac{\delta}{\sqrt{2}}. \quad (53)$$

This is a generalization of the criterion (49) for the undistorted case  $\delta = 0$ . Based on the criterion (53), one therefore expects the zero-mode degeneracy to be partially lifted at  $\delta \simeq \sqrt{2} - 1/4\beta$  [that is  $\delta \sim -3$  for our above choice  $\beta = 0.06$ ], in good agreement with the numerical results depicted in Fig. 8. Directly at the merging transition, that is for  $\delta = -c/4b\sqrt{eB}$ , one obtains a LL spectrum with levels that scale as  $\epsilon_n = 2A\beta^{1/2}(n + 1/2)^{2/3}$  with  $A = \pi[3/\Gamma(1/4)]^{2/3} \simeq 1.173$ , in agreement with the merging transition of Dirac cones with opposite Berry phases.<sup>22,23</sup> Upon a further decrease of  $\delta$ , the merging of the cones  $A$  and  $D$  is associated with a gap opening [see Fig. 3(b)] such that the corresponding LL spectrum is shifted to higher energies, as may be seen on the left-hand side in Fig. 14(b). Apart from the shift to higher energies, these LLs corresponding to the merged points scale linearly in the LL index  $n$ , as one expects for parabolic bands [ $\mathcal{A}(E) \propto E \propto n$ ]. Because of the distance in energy from the saddle points, the semiclassical approximation agrees well with the numeric spectrum, as can be checked in Fig. 9.

### D. Triple-merging transition $\delta \gg 1$

In the opposite limit, for  $\delta > 0$ , the  $A$  cone remains apart and its Fermi velocity  $v_A$  is increased. The energy of the LLs is therefore enhanced and well described within the semiclassical approximation, as may be seen in Fig. 9. The  $A$  cone is unaffected by the transition line indicating the saddle point  $\epsilon_S$  because it is not involved in the triple-merging process, as opposed to  $B$ ,  $C$ , and  $D$ , that form a boomerang-shaped

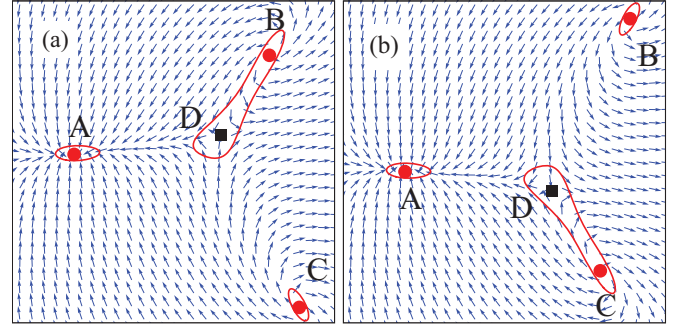


FIG. 15. (Color online) An imaginary value of  $\Delta$  ( $\theta = \pi/2$ ) induces a merging between the  $B$  and  $D$  cones [(a) for  $\text{Im}(\Delta) > 0$ ] or between the  $C$  and  $D$  cones [(b) for  $\text{Im}(\Delta) < 0$ ].

Fermi surface. The latter become coupled through the Lifshitz transition at  $E_S$ , as can be observed from the departure from the semiclassical approximation in Fig. 9. Before this transition, all three Fermi pockets increase in size, with a higher rate for  $B$  and  $C$  than for  $D$ , such that the twofold degenerate LLs corresponding to the points  $B$  and  $C$  decrease faster in energy than those of the central cone  $D$ .

There are only two zero-energy LLs since the total  $+1$  topological charge of the boomerang pocket gives rise to a unique topologically protected mode. Equivalently, the magnetic field has reached such a value that the total winding number  $w_p$  is the only relevant quantity.

Precisely at the triple merging point ( $E_S = 0$ ), the LL scale as  $n^{3/4}$  [blue dots in Fig. 8(b)], as far as our numerical accuracy is concerned. After the triple merging transition, the LL of  $D = B = C$  scale with a different power law, almost linear in  $n$ . Increasing  $\delta$  increases the energies of all the LL because of a decrease of the combined-orbit area.

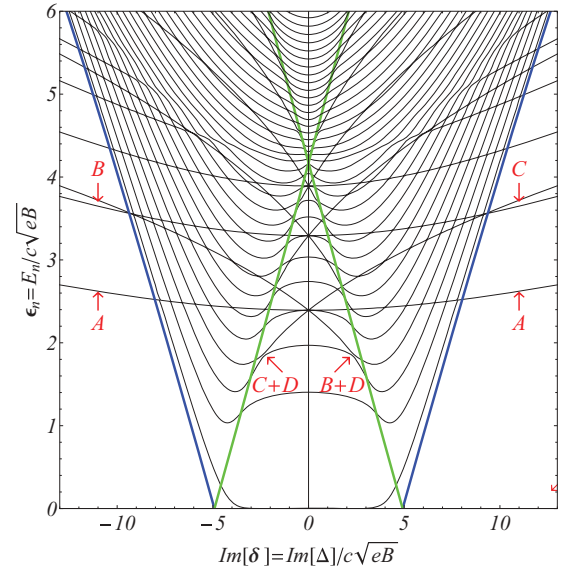


FIG. 16. (Color online) Landau level spectrum for  $\theta = \pi/2$  ( $\beta = 0.06$ ). In this case, the spectrum is symmetric in the displacement  $\text{Im}(\delta) = \text{Im}(\Delta)/c\sqrt{eB}$ . The saddle point energies are indicated by the green curves and the energy of the local gap beyond merging is indicated by the blue curves.

### E. LL spectrum for an imaginary value of $\delta$

For the sake of completeness, we present here a LL spectrum for a purely imaginary  $\Delta$  in the case of a deformation in the  $x$  axis ( $\theta = \pi/2$  in Fig. 16, see Sec. II C 3). Then, the two directions of deformation [ $\pm \text{Im}(\Delta)$ ] are equivalent, as pictured in Figs. 6(b) and 15, so that the saddle point energy and the LL spectrum is now symmetric in  $\text{Im}(\Delta)$ , as seen in Fig. 16. When  $\text{Im}(\Delta) > 0$ , the cones  $B$  and  $D$  merge leaving the cones  $A$  and  $C$  isolated, whereas for  $\text{Im}(\Delta) < 0$ , the role of the  $B$  and  $C$  points is interchanged. In a magnetic field, one distinguishes the LL sequence from the four cones below the saddle point energy, as well as the Lifshitz transition near the saddle points. Notice that the accidental degeneracy of the  $B$  and  $C$  cones, which we have encountered for real values of  $\Delta$ , is now lifted and that the LLs associated with the  $A$  cone are symmetric in  $\text{Im}(\Delta)$  (see Fig. 16). Indeed, the  $A$  cone remains isolated and does not take part in the merging transition for any value of  $\text{Im}(\Delta)$ . Its LL spectrum therefore remains relativistic with the typical  $\sqrt{n}$  scaling. In the merging sector, for energies in between the two saddle points, the  $C$  cone provides an additional set of relativistic LLs for  $\text{Im}(\Delta) > 0$ , whereas this set is provided by the  $B$  cone for  $\text{Im}(\Delta) < 0$ . As in the case of the merging transition discussed in Sec. V C, beyond  $|\Delta_m| = (c^2/4b)(6\sqrt{3} - 9)^{1/2} \simeq 1.18c^2/4b$  ( $|\delta_m| \simeq 4.92$ , for  $\beta = 0.06$  as shown in Fig. 15) the merged cones [ $B$  and  $D$  for  $\text{Im}(\Delta) > 1.18c^2/4b$  or  $C$  and  $D$  for  $\text{Im}(\Delta) < -1.18c^2/4b$ ] are accompanied by the opening of a local gap the  $\delta$  dependence of which is indicated by the thick blue line in Fig. 16. Consequently, the associated LLs are nonrelativistic with a linear- $n$  scaling because of the annihilation of the winding numbers of the merged cones.

### F. Consequences for magneto-transport measurements

We finish this section with a brief discussion of the consequences of the above picture for magneto-transport measurements, namely, in the context of Hall quantization. Such experiments have been performed both in bilayer graphene in the low-energy limit<sup>12</sup> as well as in samples with a twist between the two layers.<sup>43,44</sup> Remember that the model (8) investigated above also accounts for the case of twisted bilayer graphene, with moderate twist angles, if one sets  $c = 0$  or in the limit  $c^2/b \ll \Delta$ . In this case,  $\Delta$  is a function of the twist angle.

In all measurements, an eightfold degeneracy of the zero-energy level, with no additional quantum-Hall plateaus in the range  $-4 < \nu < 4$ , has been observed. This indicates, in addition to the usual fourfold spin-valley degeneracy, a twofold degeneracy of the zero-energy level. In the case of twisted bilayer graphene,<sup>43,44</sup> this is an indication for the twofold topological degeneracy associated with two Dirac points characterized by a unit winding number with the same sign.<sup>17</sup> For a bilayer sample with no twist,<sup>12</sup> the observed eightfold degeneracy indicates a prominent non-zero value of  $\Delta$  since one would expect, based on the above arguments for  $\Delta \sim 0$ , a 16-fold degeneracy of the zero-energy level, i.e., no quantum-Hall plateaus in between  $-8 < \nu < 8$ . It has been argued that the rather large value of  $\Delta$  cannot be explained by strain (or a displacement of the two layers) alone and that

interaction effects are likely to play an important role<sup>12</sup> in which case  $\Delta$  plays the role of a (nematic) order parameter.<sup>32</sup>

In higher LLs in trigonally-warped bilayer graphene, the degeneracy depends both on the value of the saddle point energy  $\sim |\Delta|$  as compared to the magnetic energy scale  $c\sqrt{eB}$ , as well as on the phase  $\theta$  of  $\Delta = |\Delta|\exp(i\theta)$ . In the low-energy sector (L), we have shown that for a real value of  $\Delta$  ( $\theta = 0$  or  $\pi$ , modulo  $2\pi/3$ ), the Dirac cones at  $B$  and  $C$  are related by mirror symmetry and their LLs are thus ( $2 \times 4$ )-fold degenerate in the low-energy (L) and merging (M) sectors. One would therefore expect a jump of  $\Delta\nu = 8$  in the Hall conductance whenever the Fermi level crosses such a level, whereas the LLs associated with the points  $A$  and  $D$  are only spin-valley degenerate, associated with a jump  $\Delta\nu = 4$ . Notice that the mirror symmetry is immediately broken in the case of a nonzero imaginary part of  $\Delta$ , i.e., when  $\theta \neq 0$  or  $\pi$  (modulo  $2\pi/3$ ), such that all LLs are then fourfold spin-valley degenerate only. This fourfold degeneracy is also the generic case in the other energy sectors ( $M'$  and  $H$ ). Experimentally, quantum-Hall features have been observed at  $\nu = \pm 4, \pm 8, \pm 12, \dots$ ,<sup>12</sup> such that the LLs are only spin-valley degenerate. Whereas this sequence is identical to that of bilayer graphene without trigonal warping, the  $\sqrt{B}$  scaling of the gap between the zero-energy level and the first excited one indicates that the low-energy sector is nevertheless governed by Dirac cones with a linear dispersion relation, as one would expect in the sectors  $M$  and  $M'$ .

The situation is different in twisted bilayer graphene, where one expects eightfold-degenerate LLs below the saddle point at  $E \ll |\Delta|$ , whereas they are fourfold-degenerate at  $E \gtrsim |\Delta|$ . Since the value  $|\Delta|$  can be tuned to great extent by the twist angle, one may expect to see this crossover more easily than in trigonally warped bilayer graphene. From an experimental point of view, Lee *et al.*<sup>43</sup> investigated an epitaxially grown sample on SiC, with typical twist angles of  $2.2^\circ$ . In this sample, an eightfold degeneracy of the zero-energy level has been observed, whereas higher LLs are fourfold spin-valley degenerate, that is a filling-factor sequence of  $\nu = \pm 4, \pm 8, \pm 12, \dots$  Sanchez-Yamagishi *et al.* have investigated a twisted bilayer sample fabricated by PMMA-transfer technique of two monolayer samples on hexa boron nitride.<sup>44</sup> In this case, the observed sequence of quantum-Hall plateaus is  $\nu = \pm 4, \pm 12, \pm 20, \dots$ , that is, eightfold-degenerate Landau levels also at higher energy. This indicates a large value of  $|\Delta|$  and of relatively large twist angles.

## VI. CONCLUSIONS

In conclusion, we have investigated a continuum model that accounts for the presence of two and more Dirac points in the dispersion relation. The model describes the low-energy physical properties of bilayer graphene with a stacking default, either a translational displacement of one graphene layer with respect to the other one, as compared to the perfectly AB-stacked case, or strain.<sup>15,25</sup> Furthermore, this model also accounts for a rotational stacking default (twist) if one neglects the linear term  $\mathcal{H}_c$  in the low-energy Hamiltonian (8).<sup>17</sup> Whereas the number of Dirac points is determined by the interplay between the different microscopic parameters, the total

winding number of +2 topologically guarantees the presence of at least two Dirac points (with winding number +1) or a single parabolic band-contact point (with winding number +2).

In the presence of a magnetic field and Landau quantization, the winding number yields a doubly degenerate zero-energy level that is topologically protected. We have studied the LL spectrum in the framework of a semiclassical treatment and find that it describes accurately the numerically obtained one in a large parameter range. The semiclassical theory allows for a detailed understanding of the LL spectrum in the sense that one may associate certain levels with particular Dirac points and determine the degeneracy of the levels. Furthermore, the degeneracy lifting is understood in terms of connections between Fermi pockets.

However, the semiclassical approximation, which is based on a quantization of reciprocal-space orbits and the topological charge (i.e., the winding number), breaks down in the vicinity of saddle points in the (zero-field) dispersion relation as well as at zero energy in the high-magnetic-field limit. The physical origin of this breakdown is the definition of the topological charges in terms of closed reciprocal-space orbits, which change abruptly at the saddle points when two or more Fermi pockets become connected. Indeed, the definition of topological charges needs to be revisited in the presence of a magnetic field that quantizes reciprocal space into patches

of size  $\sim 1/l_B^2 \propto B$  because the components of the kinetic-momentum operator no longer commute. This effect blurs the reciprocal-space orbits and smoothens the abrupt change in the winding number at the saddle points.

Another effect of this magnetic blurring concerns the zero-energy states. Because reciprocal-space orbits need to enclose minimal surfaces of  $\sim 1/l_B^2$ , neighboring Dirac points at zero energy are no longer resolved individually in the high-field limit. This effect is at the origin of a magnetic-field-induced Lifshitz transition, where the degeneracy of the zero-energy level, which consists of four ( $w_i = 4$ )  $n = 0$  LLs (associated with the total sum  $w_i$  of Dirac points), is partially lifted when increasing the magnetic field. Eventually, the degeneracy of the zero-energy level is then given by the total topological charge, that is  $w_p = |\sum_i w_i|$ , in terms of the zero-field winding number  $w_i = \pm 1$  of a single Dirac point.

### ACKNOWLEDGMENTS

We acknowledge fruitful discussions with Antonio H. Castro Neto, Jean-Noël Fuchs, Kostya Novoselov, and Frédéric Piéchon. This work was supported by the ANR project NANOSIM GRAPHENE under Grant No. ANR-09-NANO-016 and by the Ecole Doctorale de Physique de la Région Parisienne (ED 107).

- 
- <sup>1</sup>A. H. Castro Neto, F. Guinea, N. M. R. Peres, K. S. Novoselov, and A. K. Geim, *Rev. Mod. Phys.* **81**, 109 (2009).
- <sup>2</sup>M. Z. Hasan and C. L. Kane, *Rev. Mod. Phys.* **82**, 3045 (2010).
- <sup>3</sup>X.-L. Qi and S.-C. Zhang, *Rev. Mod. Phys.* **83**, 1057 (2011).
- <sup>4</sup>J.-N. Fuchs, F. Piéchon, M. O. Goerbig, and G. Montambaux, *Eur. Phys. J. B* **77**, 351 (2010).
- <sup>5</sup>M. I. Katsnelson, *Phys. Rev. B* **74**, 201401 (2006).
- <sup>6</sup>P.-E. Allain and J.-N. Fuchs, *Eur. Phys. J. B* **83**, 301 (2011).
- <sup>7</sup>M. O. Goerbig, *Rev. Mod. Phys.* **83**, 1193 (2011).
- <sup>8</sup>E. McCann and V. I. Fal'ko, *Phys. Rev. Lett.* **96**, 086805 (2006).
- <sup>9</sup>K. S. Novoselov, E. McCann, S. V. Morozov, V. I. Fal'ko, Katsnelson, U. Zeitler, D. Jiang, F. Schedin, and A. K. Geim, *Nat. Phys.* **2**, 177 (2006).
- <sup>10</sup>I. M. Lifshitz, *Zh. Eksp. Teor. Fiz.* **38**, 1565 (1960) [*Sov. Phys. JETP* **11**, 1130 (1960)].
- <sup>11</sup>Y. Lemonik, I. L. Aleiner, C. Toke, and V. I. Fal'ko, *Phys. Rev. B* **82**, 201408 (2010).
- <sup>12</sup>A. S. Mayorov, D. C. Elias, M. Mucha-Kruczynski, R. V. Gorbachev, T. Tudorovskiy, A. Zhukov, S. V. Morozov, M. I. Katsnelson, V. I. Fal'ko, A. K. Geim, and K. S. Novoselov, *Science* **333**, 860 (2011).
- <sup>13</sup>M. Orlita, P. Neugebauer, C. Faugeras, A.-L. Barra, M. Potemski, F. M. D. Pellegrino, and D. M. Basko, *Phys. Rev. Lett.* **108**, 017602 (2012).
- <sup>14</sup>J. M. B. Lopes dos Santos, N. M. R. Peres, and A. H. Castro Neto, *Phys. Rev. Lett.* **99**, 256802 (2007).
- <sup>15</sup>Y.-W. Son, S.-M. Choi, Y. P. Hong, S. Woo, and S.-H. Jhi, *Phys. Rev. B* **84**, 155410 (2011).
- <sup>16</sup>R. Bistritzer and A. H. MacDonald, *PNAS* **108**, 12233 (2011).
- <sup>17</sup>R. de Gail, M. O. Goerbig, F. Guinea, G. Montambaux, and A. H. Castro Neto, *Phys. Rev. B* **84**, 045436 (2011).
- <sup>18</sup>Y. Hasegawa, R. Konno, H. Nakano, and M. Kohmoto, *Phys. Rev. B* **74**, 033413 (2006).
- <sup>19</sup>S.-L. Zhu, B. Wang, and L.-M. Duan, *Phys. Rev. Lett.* **98**, 260402 (2007).
- <sup>20</sup>P. Dietl, F. Piéchon, and G. Montambaux, *Phys. Rev. Lett.* **98**, 236405 (2008).
- <sup>21</sup>B. Wunsch, F. Sols, and F. Guinea, *New J. Phys.* **10**, 103027 (2008).
- <sup>22</sup>G. Montambaux, F. Piéchon, J.-N. Fuchs, and M. O. Goerbig, *Phys. Rev. B* **80**, 153412 (2009).
- <sup>23</sup>G. Montambaux, F. Piéchon, J.-N. Fuchs, and M. O. Goerbig, *Eur. Phys. J. B* **72**, 509 (2009).
- <sup>24</sup>C. Lee, X. Wei, J. K. Kysar, and J. Hone, *Science* **321**, 385 (2008).
- <sup>25</sup>M. Mucha-Kruczynski, I. L. Aleiner, and V. I. Fal'ko, *Phys. Rev. B* **84**, 041404 (2011).
- <sup>26</sup>E. J. Mele, *Phys. Rev. B* **84**, 235439 (2011).
- <sup>27</sup>R. de Gail, J.-N. Fuchs, M. Goerbig, F. Piéchon, and G. Montambaux, *Physica B: Cond. Mat.* **407**, 1948 (2012).
- <sup>28</sup>J. Hass, F. Varchon, J. E. Millán-Otoya, M. Sprinkle, N. Sharma, W. A. de Heer, C. Berger, P. N. First, L. Magaud, and E. H. Conrad, *Phys. Rev. Lett.* **100**, 125504 (2008).
- <sup>29</sup>M. Mucha-Kruczynski, I. L. Aleiner, and V. I. Fal'ko, *Solid State Commun.* **151**, 1088 (2011).
- <sup>30</sup>K. Zou, X. Hong, and J. Zhu, *Phys. Rev. B* **84**, 085408 (2011).
- <sup>31</sup>J. L. Mañes, F. Guinea, and M. A. H. Vozmediano, *Phys. Rev. B* **75**, 155424 (2007).
- <sup>32</sup>O. Vafek and K. Yang, *Phys. Rev. B* **81**, 041401 (2010).
- <sup>33</sup>M. V. Berry, *Proc. R. Soc. London, Ser. A* **392**, 45 (1984).
- <sup>34</sup>L. A. Falkovsky, *Zh. Eksp. Teor. Fiz.* **49**, 609 (1965) [*Sov. Phys. JETP* **22**, 423 (1965)].

- <sup>35</sup>C.-H. Park and N. Marzari, *Phys. Rev. B* **84**, 205440 (2011).
- <sup>36</sup>A. Ozerin and L. Falkovsky, arXiv:1203.0157v1.
- <sup>37</sup>J. M. Pereira Jr., F. M. Peeters, and P. Vasilopoulos, *Phys. Rev. B* **76**, 115419 (2007).
- <sup>38</sup>L. Onsager, *Philos. Mag.* **43**, 1006 (1952).
- <sup>39</sup>I. M. Lifshitz and A. M. Kosevich, *Zh. Eksp. Teor. Fiz.* **29**, 730 (1960) [*Sov. Phys. JETP* **2**, 636 (1955)].
- <sup>40</sup>M. Wilkinson, *J. Phys. A* **17**, 3459 (1984).
- <sup>41</sup>G. P. Mikitik and Y. V. Sharlai, *Phys. Rev. Lett.* **82**, 2147 (1999).
- <sup>42</sup>G. E. Volovik, *The Universe in a Helium Droplet* (Clarendon Press, Oxford, 2003).
- <sup>43</sup>D. S. Lee, C. Riedl, T. Beringer, A. H. Castro Neto, K. von Klitzing, U. Starke, and J. H. Smet, *Phys. Rev. Lett.* **107**, 216602 (2011).
- <sup>44</sup>J. D. Sanchez-Yamagishi, T. Taychatanapat, K. Watanabe, T. Taniguchi, A. Yacoby, and P. Jarillo-Herrero, *Phys. Rev. Lett.* **108**, 076601 (2012).